Quasiequilibrium sequences of binary neutron stars undergoing dynamical scalarization

Keisuke Taniguchi,[1] Masaru Shibata,[2] and Alessandra Buonanno[3,4]

[1]*Graduate School of Arts and Sciences, University of Tokyo, Komaba, Meguro, Tokyo 153-8902, Japan*
[2]*Yukawa Institute for Theoretical Physics, Kyoto University, Kyoto 606-8502, Japan*
[3]*Max Planck Institute for Gravitational Physics (Albert Einstein Institute), Am Mühlenberg 1, Potsdam-Golm 14476, Germany*
[4]*Department of Physics, University of Maryland, College Park, Maryland 20742, USA*

(Received 2 October 2014; published 23 January 2015)

We calculate quasiequilibrium sequences of equal-mass, irrotational binary neutron stars in a scalar-tensor theory of gravity that admits dynamical scalarization. We model neutron stars with realistic equations of state (notably through piecewise polytropic equations of state). Using these quasiequilibrium sequences we compute the binary's scalar charge and binding energy versus orbital angular frequency. We find that the absolute value of the binding energy is smaller than in general relativity, differing at most by ∼14% at high frequencies for the cases considered. We use the newly computed binding energy and the balance equation to estimate the number of gravitational-wave (GW) cycles during the adiabatic, quasicircular inspiral stage up to the end of the sequence, which is the last stable orbit or the mass-shedding point, depending on which comes first. We find that, depending on the scalar-tensor parameters, the number of GW cycles can be substantially smaller than in general relativity. In particular, we obtain that when dynamical scalarization sets in around a GW frequency of ∼130 Hz, the sole inclusion of the scalar-tensor binding energy causes a reduction of GW cycles from ∼120 Hz up to the end of the sequence (∼1200 Hz) of ∼11% with respect to the general-relativity case. (The number of GW cycles from ∼120 Hz to the end of the sequence in general relativity is ∼270.) We estimate that when the scalar-tensor energy flux is also included the reduction in GW cycles becomes of ∼24%. Quite interestingly, dynamical scalarization can produce a difference in the number of GW cycles with respect to the general-relativity point-particle case that is much larger than the effect due to tidal interactions, which is on the order of only a few GW cycles. These results further clarify and confirm recent studies that have evolved binary neutron stars either in full numerical relativity or in post-Newtonian theory, and point out the importance of developing accurate scalar-tensor-theory waveforms for systems composed of strongly self-gravitating objects, such as binary neutron stars.

DOI: 10.1103/PhysRevD.91.024033 PACS numbers: 04.20.Ex, 04.30.Db, 04.40.Dg, 04.50.Kd

I. INTRODUCTION

Coalescing binary neutron stars are among the most promising sources of gravitational waves (GWs) for the next-generation, kilometer-size, GW detectors such as advanced LIGO [1], advanced Virgo [2], and KAGRA [3]. Binary neutron stars, together with black-hole–neutron-star binaries, are also regarded as one of the candidate central engines of short-hard gamma-ray bursts [4]. The use of the matched-filtering technique to detect GW signals from coalescing binary systems and the interest in shedding light on gamma-ray burst progenitors have led to impressive advances in modeling the dynamics and gravitational waveforms of binary neutron stars (see, e.g., Ref. [5] for the inspiral phase and Refs. [6–8] for the merger and postmerger phases). Most of those studies were carried out in general relativity, except for Refs. [9–11]. Although general relativity has passed all known experimental and observational tests in the weak-field and slow-motion limit (see, e.g., Ref. [12]), it remains to be seen whether it will survive tests in the strong-field and high-velocity regime.

The detection of GWs emitted by coalescing binary systems offers the unique opportunity to investigate the validity of general relativity in the strong-field regime. To achieve this goal, accurate gravitational waveforms in gravity theories alternative to general relativity [12–14] need to be computed. Here we follow our recent work [10] and focus on the scalar-tensor model [15–18] proposed by Damour and Esposito-Farèse (DEF) [19] (see also Refs. [20–22]). Quite interestingly, there exist choices of the free parameters in the DEF model, for which both weak and mildly strong gravitational tests are satisfied, notably the pulsar timing tests, but strong-field tests could be violated and these violations could be observed through the emission of GWs from the last stages of the binary's inspiral, plunge, and merger in advanced LIGO, Virgo, and KAGRA detectors. This is possible because if neutron stars in binary systems carry negligible scalar charge when largely separated, they can be dynamically scalarized as

they come closer to each other through gravitational interaction; i.e., they undergo dynamical scalarization as the binary's compactness increases [9–11]. (See also Refs. [23–25] for scalarization of rotating stars.) However, it is important to notice that for the same values of the DEF parameters for which dynamical scalarization can occur, the DEF model may have problems in providing cosmological solutions consistent with our Universe [26–28]. It will be relevant to further investigate this problem in the future.

Barausse *et al.* [9] showed that dynamical scalarization takes place in the DEF model by performing numerical-relativity simulations of inspiraling binary neutron stars. They performed two numerical simulations, which differed by the strength of the scalar field and the binary's mass ratio. Their simulations used approximate initial data, i.e., initial data computed by numerical codes of general relativity instead of the ones of scalar-tensor theory, and employed the polytropic equation of state $p/c^2 = K\rho_0^\Gamma$ with $\Gamma = 2$ and $K = 123G^3M_\odot^2/c^6$, where p is the pressure and ρ_0 is the baryonic rest-mass density in their notation. For the unequal-mass binary the individual baryonic rest masses were $1.78M_\odot$ and $1.90M_\odot$, while for the equal-mass binary the baryonic rest mass was $1.625M_\odot$.[1]

For comparison, we computed not in general relativity but in the DEF scalar-tensor theory the initial data for the same baryonic rest masses used in Barausse *et al*. We set $\beta/(4\pi G) = -4.5$ and $\varphi_{0,\mathrm{BPPL}} = 10^{-5}G^{-1/2}$, where β is a constant related to the derivative of a scalar field and $\varphi_{0,\mathrm{BPPL}}$ is the asymptotic value of the scalar field as defined by Barausse *et al.* [9]. We found that the more massive star (with baryonic rest mass of $1.90M_\odot$) is spontaneously scalarized for a spherical configuration, and thus, the unequal-mass binary system is already scalarized at the orbital separation of 60 km, which is where Ref. [9] starts their simulations (see Appendix A for more details). Because in their simulation the scalar field does not exist initially, it rapidly increases just after the simulation starts. This artificial behavior may have left imprints in the dynamical evolution of the binary system. Indeed, as we will see in Sec. III, the binding energy computed along a sequence of quasiequilibrium configurations in the DEF scalar-tensor theory is in absolute value smaller than in general relativity. Thus, as soon as the simulation starts, if initial data without the scalar field are used, which is the case in Barausse *et al.*, then the absolute value of the binding energy will become smaller because the scalar field increases. This means that the initial datum is a local minimum of the binding energy along the quasiequilibrium sequences; i.e., it is a local turning point of the binding energy. We suspect that the fast plunge seen in Ref. [9] might be enhanced by this effect. Performing a numerical simulation using general-relativity and scalar-tensor-theory initial data will clarify this point.

For the equal-mass binary system numerically evolved in Ref. [9] we found, using quasiequilibrium configurations, that the binary is already dynamically scalarized at the orbital separation of 40 km where Ref. [9] observed dynamical scalarization. However, our result of an earlier dynamical scalarization may not be in contradiction with Ref. [9]. Indeed, typically we found that the onset of dynamical scalarization in the quasiequilibrium-configuration study occurs earlier than that in dynamical simulation [10]. This discrepancy may occur due to the breakdown of the assumption of quasiequilibrium. For a few orbits before merger the infall velocity of each star in the binary system is larger in numerical-relativity simulations than in quasiequilibrium configurations. As a consequence, in numerical-relativity simulations the binary can merge before the scalar field reaches its equilibrium state, while, in the quasiequilibrium situation, the scalar field can reach its equilibrium state even just before the quasiequilibrium sequence ends. Thus, the effect of the scalar field is overestimated in the quasiequilibrium study for the cases in which dynamical scalarization occurs just before the end of the quasiequilibrium sequences. We will present more details about the results of the equal-mass binary in Appendix A.

More recently, Palenzuela *et al.* [11] investigated analytically the phenomenon of dynamical scalarization in the DEF model. They employed the 2.5 post-Newtonian (PN) equations of motion, recently derived in Ref. [30], augmented by a set of equations that phenomenologically describe the increase of scalar charge as the two neutron stars come closer to each other. In this analysis the binary neutron stars are approximated by two isolated, spherical neutron stars. Reference [11] confirmed and quantified what was found in Refs. [9,10], notably the fact that binary neutron stars plunge and merge in the DEF model sooner than in general relativity when they undergo induced and dynamical scalarization.

To further understand the onset of dynamical scalarization during the last stages of inspiral, we disentangle conservative from radiative effects and compute for the first time quasiequilibrium sequences of binary neutron stars in the DEF model. Our motivations are threefold. We want to (i) produce initial data for merger simulations in the scalar-tensor model [10], (ii) accurately extract physical quantities (notably the binding energy and angular momentum) during the last stages of inspiral, just before merger, where the effect of gravity becomes strong and the finite-size effect of a neutron star starts to affect the evolution of the binary system, and (iii) use those quantities to estimate by how much the gravitational waveforms in the DEF model differ from the ones in general relativity.

[1]We notice that due to a misleading output in the LORENE data set [29], the gravitational masses are not the ones reported in Ref. [9]. The gravitational masses of spherical, isolated stars corresponding to the baryonic rest masses of $1.625M_\odot$, $1.78M_\odot$, and $1.90M_\odot$ are $1.51M_\odot$, $1.64M_\odot$, and $1.74M_\odot$, respectively. The results of Ref. [9] are correct; i.e., they were not affected by the gravitational masses reported in the paper.

This paper is organized as follows. In Sec. II, we give a brief summary of the quasiequilibrium-sequence formalism. The formulation is based on the conformal thin-sandwich decomposition. In Sec. III we present and discuss the numerical results of the scalar charge and scalar mass, binding energy, total angular momentum, central baryonic rest-mass density, evolution of the orbital angular frequency, and number of GW cycles. Section IV summarizes our main conclusions.

Throughout this paper, we employ the geometrical units of $c = G = 1$, where c is the speed of light and G is the bare gravitational constant. We use greek letters to denote spacetime components and latin letters for the spatial components.

II. FORMULATION

As in Ref. [10], we work in the Jordan frame [15,17]. The basic field equations for computing the metric quantities and the scalar field are derived by taking variation of the action,

$$\mathcal{S} = \frac{1}{16\pi}\int [\phi R - \omega(\phi)\phi^{-1} g^{\mu\nu}(\nabla_\mu\phi)(\nabla_\nu\phi)]\sqrt{-g}d^4x + \mathcal{S}_{\rm matter}, \tag{1}$$

where ϕ is the scalar field, $g_{\mu\nu}$ is the spacetime metric in the Jordan frame, R is the Ricci scalar calculated from $g_{\mu\nu}$, g is the determinant of $g_{\mu\nu}$, ∇_μ is the covariant derivative with respect to $g_{\mu\nu}$, and $\mathcal{S}_{\rm matter}$ is the matter part of the action. The quantity ω is a function of ϕ that takes the form

$$\frac{1}{\omega(\phi)+3/2} = B\ln\phi \tag{2}$$

in the DEF theory, where B is a free parameter [19] (see Ref. [10] for more details). The relation between Newton's constant $G_{\rm N}$ and the bare gravitational constant G is

$$G_{\rm N} = \frac{G}{\phi_0}\frac{4+2\omega(\phi_0)}{3+2\omega(\phi_0)}, \tag{3}$$

where ϕ_0 is the value of ϕ at spatial infinity. For the values used in this paper, the deviation of the ratio $G_{\rm N}/G$ from unity is on the order of $10^{-9} - 10^{-10}$ [see Eq. (16) and the scalar-tensor values listed at the end of Sec. II].

Taking variation of the action (1) with respect to the metric and the scalar field, we obtain

$$R_{\mu\nu} - \frac{1}{2}Rg_{\mu\nu} = 8\pi\phi^{-1}T_{\mu\nu} + \omega\phi^{-2}\left[(\nabla_\mu\phi)(\nabla_\mu\phi) - \frac{1}{2}g_{\mu\nu}(\nabla_\alpha\phi)(\nabla^\alpha\phi)\right] + \phi^{-1}(\nabla_\mu\nabla_\nu\phi - g_{\mu\nu}\Box\phi) \tag{4}$$

and

$$\Box\phi = \frac{1}{2\omega+3}\left[8\pi T - \frac{d\omega}{d\phi}(\nabla_\mu\phi)(\nabla^\mu\phi)\right], \tag{5}$$

respectively, where $R_{\mu\nu}$ is the Ricci tensor, $\Box$ is $\nabla_\mu\nabla^\mu$, and $T_{\mu\nu}$ is the stress-energy tensor. For an ideal fluid we have

$$T_{\mu\nu} = (\rho + \rho\varepsilon + P)u_\mu u_\nu + Pg_{\mu\nu}, \tag{6}$$

where u_μ is the fluid 4-velocity, ρ is the baryonic rest-mass density, ε is the specific internal energy, and P is the pressure. Then, we set the metric line element in $3+1$ form,

$$\begin{aligned} ds^2 &= g_{\mu\nu}dx^\mu dx^\nu, \\ &= -\alpha^2dt^2 + \gamma_{ij}(dx^i + \beta^i dt)(dx^j + \beta^j dt) \end{aligned} \tag{7}$$

where α is the lapse function, β^i is the shift vector, and γ_{ij} is the spatial part of the spacetime metric, and we solve the basic field equations in the conformal thin-sandwich decomposition [31,32]. We decompose the equations for the metric quantities (4) into the *Hamiltonian* constraint,

$$\begin{aligned} {}^{(3)}R + K^2 - K_{ij}k^{ij} = {}& 16\pi\phi^{-1}\rho_{\rm h} \\ &+ \omega\phi^{-2}[\Pi^2 + (D_\alpha\phi)(D^\alpha\phi)] \\ &+ 2\phi^{-1}(D_\mu D^\mu\phi - K\Pi), \end{aligned} \tag{8}$$

and the *momentum* constraint,

$$\begin{aligned} D_iK^i_j - D_jK = {}& 8\pi\phi^{-1}J_j + \omega\phi^{-2}\Pi D_j\phi \\ &+ \phi^{-1}(D_j\Pi - K^i_jD_i\phi); \end{aligned} \tag{9}$$

furthermore the trace part of the evolution equation for the extrinsic curvature K_{ij} satisfies the following equation

$$\begin{aligned} &(\partial_t - \beta^k\partial_k)K \\ &\quad = 4\pi\alpha\phi^{-1}(\rho_{\rm h} + S) + \alpha K_{ij}K^{ij} - D_iD^i\alpha \\ &\qquad + \alpha\omega\phi^{-2}\Pi^2 + \alpha\phi^{-1}D_iD^i\phi - \alpha\phi^{-1}K\Pi \\ &\qquad - \frac{3\alpha\phi^{-1}}{2(2\omega+3)}\left[8\pi T + \frac{d\omega}{d\phi}\left\{\Pi^2 - (D_k\phi)(D^k\phi)\right\}\right], \end{aligned} \tag{10}$$

while the evolution equation for the spatial metric reads

$$\partial_t\gamma_{ij} = -2\alpha K_{ij} + \gamma_{kj}D_i\beta^k + \gamma_{ik}D_j\beta^k, \tag{11}$$

where ${}^{(3)}R$ denotes the Ricci scalar calculated from γ_{ij}, D_i the covariant derivative with respect to γ_{ij}, K the trace part of the extrinsic curvature, and $\Pi \equiv -n^\mu\partial_\mu\phi$. Here the quantities $\rho_{\rm h}$, J_i, S, and T are defined as

$$\rho_{\rm h} = n_\mu n_\nu T^{\mu\nu}, \tag{12a}$$

$$J_i = -n_\mu \gamma_{\nu i} T^{\mu\nu}, \tag{12b}$$

$$S = \gamma^{ij}(\gamma_{i\mu}\gamma_{j\nu}T^{\mu\nu}), \tag{12c}$$

$$T = g_{\mu\nu}T^{\mu\nu}, \tag{12d}$$

where n^μ is the unit normal to the spatial hypersurface.

In the above decomposition, there appear four freely specified quantities: the background spatial metric, $\tilde{\gamma}_{ij}$, the time derivative of the background spatial metric in contravariant form, $\partial_t \tilde{\gamma}^{ij}$, the trace part of the extrinsic curvature, K, and its time derivative, $\partial_t K$. The background spatial metric is defined by $\tilde{\gamma}_{ij} \equiv \psi^{-4}\gamma_{ij}$ where ψ is the conformal factor. Since we consider a stationary state, we set to zero the time derivatives of the above quantities. We also set to zero the trace part of the extrinsic curvature, K, because we impose the condition of maximal slicing. We further require that the background spatial metric, $\tilde{\gamma}_{ij}$, be flat; that is, $\tilde{\gamma}_{ij} = f_{ij}$ where f_{ij} is the flat spatial metric [33–35].

The equation for the scalar field (5) is also rewritten in the conformal thin-sandwich decomposition as

$$(\partial_t - \beta^i\partial_i)\Pi = -\alpha D_i D^i\phi - (D_i\alpha)(D^i\phi) + \alpha K\Pi + \frac{\alpha}{2\omega+3}\left[8\pi T + \frac{d\omega}{d\phi}(\Pi^2 - (D_k\phi)(D^k\phi))\right]. \tag{13}$$

The above equation depends on the quantities Π and $\partial_t\Pi$. Since we consider a stationary state, we set to zero $\partial_t\Pi$. For the quantity Π, we need to guarantee that it behaves at least as $\Pi = \mathcal{O}(r^{-2})$ in the far zone. This is because the right-hand side of the Hamiltonian constraint and the trace part of the evolution equation for K_{ij} should decrease fast enough to ensure the spacetime to be asymptotically flat. In this paper, for simplicity, we set to zero the quantity Π (see Sec. II D of Ref. [10] for a more detailed discussion).

Note that, as we mentioned above, we have the freedom of choosing another background spatial metric, $\tilde{\gamma}_{ij}$, as well as the quantity Π, and the trace part of the extrinsic curvature, K. We think that the choice we made for the background spatial metric does not affect the main results of this paper, notably the onset of dynamical scalarization along quasiequilibrium binary neutron stars. As we will see in Sec. III A, the location of dynamical scalarization, i.e., the orbital angular frequency at the onset of dynamical scalarization, agrees with what is determined by fully relativistic simulations and estimated by the analytical method discussed in Ref. [10]. Because the simulations and the analytical estimation do not rely on the assumptions used in this paper, our results for the location of dynamical scalarization can be considered robust.

Thus, the equations for the quantities that enter in the metric can be recast in the form

$$\Delta\psi = -2\pi\exp(-\varphi^2/2)\psi^5\rho_{\rm h} - \frac{1}{8}\psi^{-7}\tilde{A}_{ij}\tilde{A}^{ij} - \frac{1}{2}\pi B\psi^5\varphi^2 T\exp(-\varphi^2/2) - \frac{1}{4}\psi\left(1+\frac{1}{B}-\frac{3}{4}\varphi^2\right)f^{ij}(\partial_i\varphi)(\partial_j\varphi) + \frac{1}{4}\Phi^{-1}\varphi f^{ij}(\psi\partial_i\Phi - \Phi\partial_i\psi)(\partial_j\varphi), \tag{14a}$$

$$\Delta\Phi = 2\pi\exp(-\varphi^2/2)\Phi\psi^4(\rho_{\rm h}+2S) + \frac{7}{8}\Phi\psi^{-8}\tilde{A}_{ij}\tilde{A}^{ij} - \frac{3}{2}\pi B\Phi\psi^4\varphi^2 T\exp(-\varphi^2/2) - \frac{1}{4}\Phi\left(3+\frac{1}{B}-\frac{3}{4}\varphi^2\right)f^{ij}(\partial_i\varphi)(\partial_j\varphi) - \frac{3}{4}\psi^{-1}\varphi f^{ij}(\psi\partial_i\Phi - \Phi\partial_i\psi)(\partial_j\varphi), \tag{14b}$$

$$\Delta\beta^i + \frac{1}{3}f^{ij}\partial_j(\partial_k\beta^k) = 16\pi\exp(-\varphi^2/2)\Phi\psi^{-1}f^{ij}J_j - 2\Phi\psi^{-7}\tilde{A}^{ij}(7\psi^{-1}\partial_j\psi - \Phi^{-1}\partial_j\Phi) - 2\Phi\varphi\psi^{-7}\tilde{A}^{ij}\partial_j\varphi, \tag{14c}$$

$$\tilde{A}^{ij} = \frac{\psi^7}{2\Phi}\left(f^{kj}\partial_k\beta^i + f^{ik}\partial_k\beta^j + \frac{2}{3}f^{ij}\partial_k\beta^k\right), \tag{14d}$$

where $\tilde{A}^{ij}$ is the traceless part of the conformal extrinsic curvature defined as

$$\tilde{A}^{ij} = \psi^{10}\left(K^{ij} - \frac{1}{3}\gamma^{ij}K\right), \tag{15}$$

the quantity Φ is defined as $\Phi \equiv \alpha\psi$, and we introduce a new scalar field φ which is related to the scalar field ϕ as

$$\varphi \equiv \sqrt{2\ln\phi}. \tag{16}$$

The equation for the scalar field (5) can be rewritten in the conformal thin-sandwich decomposition imposing $K = 0$, $\partial_t\Pi = 0$, and $\Pi = 0$, as

$$\Delta\varphi = 2\pi B\psi^4\varphi T\exp(-\varphi^2/2) - \varphi f^{ij}(\partial_i\varphi)(\partial_j\varphi) - f^{ij}(\Phi^{-1}\partial_i\Phi + \psi^{-1}\partial_i\psi)(\partial_j\varphi). \tag{17}$$

(See Ref. [10] for a more detailed derivation of the equations for the quantities entering the metric and the scalar field.)

We also need to solve for the relativistic hydrostatic equations, $\nabla_\mu T^{\mu\nu} = 0$, which are basically the same as in general relativity because they are written in the Jordan frame. The equations are decomposed into the first integral of the Euler equation,

$$h\alpha\frac{\gamma}{\gamma_0} = \text{const}, \tag{18}$$

and the equation of continuity,

$$\frac{\rho}{h}\nabla_\mu\nabla^\mu\Psi + (\nabla_\mu\Psi)\nabla^\mu\left(\frac{\rho}{h}\right) = 0, \tag{19}$$

where $h = (\rho + \rho\varepsilon + P)/\rho$ is the fluid specific enthalpy, γ is the Lorentz factor between the fluid and co-orbiting observers, and γ_0 is the Lorentz factor between the co-orbiting and Eulerian observers. The quantity Ψ is the fluid velocity potential, which for an irrotational fluid and an Eulerian observer is related to the fluid 3-velocity U^i as

$$U^i = \frac{\psi^{-4}}{\alpha u^t h}\tilde{\gamma}^{ij}\partial_j\Psi, \tag{20}$$

where u^t is the time component of the fluid 4-velocity (see Refs. [36–38] for more details).

We model neutron stars with realistic equations of state (EOS), using piecewise polytrope segments as introduced by Read *et al.* [39,40]. In particular, we set the number of polytrope segments to four and choose the model of APR4 and H4 in Ref. [39]. We remind readers that the APR4 EOS [41] is derived by a variational method with modern nuclear potentials among neutrons, protons, electrons, and muons. The H4 EOS [42] is derived by a relativistic mean-field theory and includes effects of hyperons. We set the internal flow in the neutron star to be irrotational as seen by an inertial observer at infinity [43].

There are two free parameters in the DEF model: (i) B, which appears in ω, and (ii) φ_0 the value of φ at spatial infinity. As discussed in Ref. [10], we choose those values, taking into account the observational constraints from neutron-star–white-dwarf binaries [44–46]. We set $\varphi_0 = 1 \times 10^{-5}$ and vary B from 8.0 to 9.0 for APR4 EOS, while $\varphi_0 = 5 \times 10^{-5}$ and B from 8.5 to 9.5 for H4 EOS.

III. NUMERICAL RESULTS

We use the spectral-method library LORENE, developed by the numerical-relativity group at the Observatory of Meudon [29], and construct a numerical code to compute quasiequilibrium configurations of binary neutron stars in the DEF model. The code is similar to those developed in Refs. [36,37,47,48] for binary neutron stars in general relativity, in particular, in Ref. [37].

We consider irrotational, equal-mass binary neutron stars whose total mass is $m = 2.7M_\odot$ at infinite separation, and we construct sequences fixing the baryonic rest mass of the two neutron stars,

$$M_{\rm B}^{(A)} = \int_{\text{star A}} \rho u^t\sqrt{-g}d^3x \quad (A = 1 \quad \text{or} \quad 2), \tag{21}$$

and varying the orbital separation. As found in Ref. [10], for both APR4 and H4 EOSs spontaneous scalarization does not occur in each star whose mass in isolation is $1.35M_\odot$. Thus, the baryonic rest masses corresponding to the mass of $1.35M_\odot$ in the scalar-tensor case are $1.50M_\odot$ for APR4 and $1.47M_\odot$ for H4, respectively. Those values are, basically, the same as those in general relativity. Note that the total mass m is the asymptotic value of the tensor mass defined by $M_{\rm T} = M_{\rm ADM} + M_{\rm S}$ [49] at infinite separation. Here $M_{\rm ADM}$ is the Arnowitt-Deser-Misner (ADM) mass and $M_{\rm S}$ is the scalar mass. The latter is defined as the monopole part of the scalar field, ϕ, which is expanded as $\phi = \phi_0 + 2M_{\rm S}/r + \mathcal{O}(1/r^2)$ for $r \to \infty$ where r is the radial coordinate. In Appendix B, we show a convergence test for the scalar mass, varying the numerical resolution (i.e., the number of collocation points).

A. Scalar charge and scalar mass

In Fig. 1 we plot the scalar charge (and scalar mass) versus the orbital angular frequency for several choices of the parameters B and φ_0. Here the scalar charge, M_φ, is defined as the monopole part of the field, φ, which is expanded as $\varphi = \varphi_0 + M_\varphi/r + \mathcal{O}(1/r^2)$ for $r \to \infty$. (Note again that in this paper we employ the geometrical units $c = G = 1$.) The relation between the scalar charge and the scalar mass is given by $M_\varphi = 2M_{\rm S}/(\phi_0\varphi_0)$.[2] We clearly see the onset of dynamical scalarization as the orbital separation (angular frequency) decreases (increases), except for the case of H4 EOS $B = 8.5$. Those results confirm what is found when evolving in full numerical relativity a binary neutron star with APR4 and H4 EOSs [10]. In particular, the onset of dynamical scalarization was well captured by the scalarization condition derived in Sec. III B of Ref. [10]. For example, Table I of Ref. [10] predicted that the dynamical scalarization for a binary system of $(1.35 + 1.35)M_\odot$ in the case of APR4 $B = 9.0$ sets in at around the orbital separation of $a \simeq 91M_\odot \simeq 134$ km. If we regard this separation as the coordinate separation of our present computation, it corresponds to the orbital angular frequency of $G_{\rm N}m\Omega \simeq 0.005$. This is confirmed by Fig. 1 where dynamical scalarization clearly occurs at around the orbital angular frequency of $G_{\rm N}m\Omega \simeq 0.005$.

In Table I we show the orbital angular frequencies and GW frequencies at the onset of dynamical scalarization. These quantities are extracted from Fig. 1 using the fit to the scalar charge obtained in Appendix C [see Eq. (C2)].

[2]Because the deviation of the quantity $\phi_0 = \exp(\varphi_0^2/2)$ from unity is on the order of $10^{-9} - 10^{-10}$ as we set $\varphi_0 = 1 \times 10^{-5}$ or $\varphi_0 = 5 \times 10^{-5}$, the relation between the scalar charge and the scalar mass is approximately given by $M_\varphi \simeq 2M_{\rm S}/\varphi_0$ (see Ref. [10] for more details).

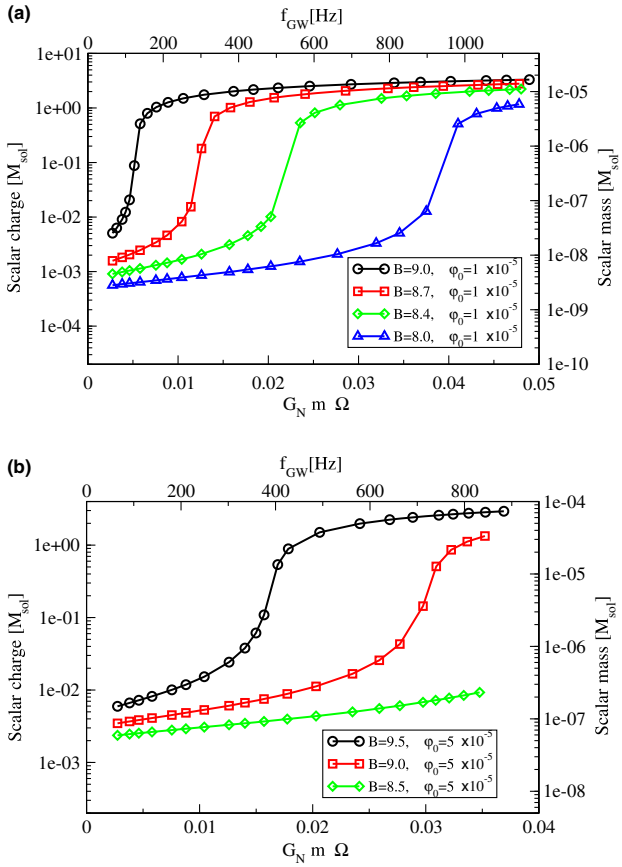

FIG. 1 (color online). Scalar charge (left y axis) or scalar mass (right y axis) as a function of the orbital angular frequency normalized to the tensor mass at infinite separation (lower x axis) or as a function of the frequency of GWs defined by $f_{\rm GW} \equiv \Omega/\pi$ from a binary neutron star with $m = 2.7M_\odot$ (upper x axis). Upper panel (a) shows results for APR4 EOS. Black solid curve with open circles, red with open squares, green with open diamonds, and blue with open triangles are, respectively, for the cases $B = 9.0, 8.7, 8.4$, and 8.0. Lower panel (b) shows results for H4 EOS. Black solid curve with open circles, red with open squares, and green with open diamonds are, respectively, for the cases $B = 9.5$, 9.0, and 8.5. (a) APR4: $1.35\,{\rm M_{sol}} - 1.35\,{\rm M_{sol}}$. (b) H4: $1.35\,{\rm M_{sol}} - 1.35\,{\rm M_{sol}}$.

(In particular, $G_{\rm N} m \Omega_{\rm dyn\text{-}scal}$ is the angular orbital frequency at which the fit function intersects 1.) From Fig. 1 we see that the scalar charge at the orbital angular frequencies listed in Table I is about $0.1M_\odot$. This value is only 4% of the total mass m; thus, at the onset of dynamical scalarization the effect of the scalar field onto the dynamics is negligible. However, as dynamical scalarization proceeds, the scalar charge rapidly increases by one order of magnitude, affecting the subsequent evolution of the binary system.

For the cases of APR4 EOS $B = 8.0$ and H4 EOS $B = 9.0$, the numerical-relativity simulations carried out in Ref. [10] showed that dynamical scalarization did not occur during the inspiral but at merger (see Table II of Ref. [10]). On the other hand, Fig. 1 predicts that for APR4 EOS

TABLE I. We list the orbital angular frequency and GW frequency ($f_{\rm GW} \equiv \Omega/\pi$) at the onset of dynamical scalarization.

Models	$G_{\rm N} m \Omega_{\rm dyn\text{-}scal}$	$f_{\rm GW,dyn\text{-}scal}$ [Hz]
APR4 (9.0)	0.0051	123
APR4 (8.7)	0.0125	298
APR4 (8.4)	0.0223	534
APR4 (8.0)	0.0395	946
H4 (9.5)	0.0163	391
H4 (9.0)	0.0302	724

$B = 8.0$ and H4 EOS $B = 9.0$ dynamical scalarization occurs before the end of the quasiequilibrium sequence. This contradiction may arise because toward the end of the inspiral the infall velocity becomes large and the quasiequilibrium model may lose accuracy.

Dynamical scalarization was first found in Ref. [9] using polytropic EOS and it was further investigated by the same authors in Ref. [11] using 2.5PN equations of motion augmented by a set of equations that phenomenologically describe the increase of scalar charge as the two neutron stars come closer to each other. Figure 3 in Ref. [11] is similar to our Fig. 1, although the former is obtained treating binary neutron stars as two, isolated spherical neutron stars and using 2PN equations of motion for circular orbits [30], instead of evolving the binary system along a sequence of quasiequilibrium configurations in the DEF model.

The results in Fig. 1 are not very sensitive to the value of φ_0. Indeed, we show in Fig. 2 that when we decrease the value of φ_0 to 1×10^{-6} for APR4 EOS, dynamical scalarization occurs at almost the same orbital angular frequency. Note that at low orbital frequencies, the scalar charge in the case $\varphi_0 = 1 \times 10^{-6}$ is one order of magnitude

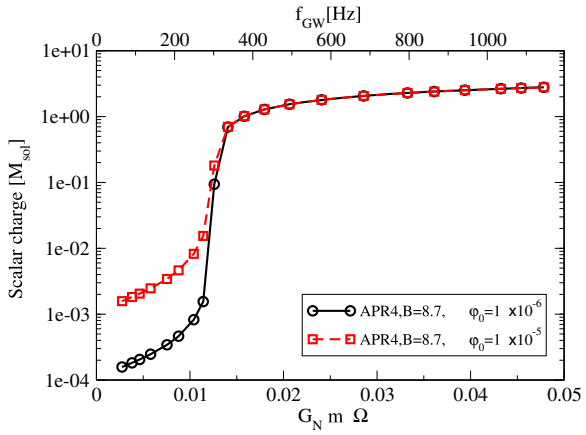

FIG. 2 (color online). Scalar charge as a function of the orbital angular frequency normalized to the tensor mass at infinite separation (lower x axis) or as a function of the frequency of GWs (upper x axis). Both curves are computed for the case of APR4 EOS $B = 8.7$, but the value of φ_0 is set to 1×10^{-5} (red dashed with open squares) and 1×10^{-6} (black solid with open circles).

smaller than in the case $\varphi_0 = 1 \times 10^{-5}$. This confirms that at large separation the scalar charge is proportional to φ_0, as found in Ref. [10]. After dynamical scalarization occurs the scalar charge has the same value, independently on φ_0.

Note that the numerically constructed quasiequilibrium sequences in Fig. 1 (also in Figs. 2–5) do not end at the onset of mass shedding from the neutron star's surface, but stop just before it. This is because it is impossible to treat a cuspy shape within the spectral method. Thus, we are obliged to stop the computation before the onset of mass shedding where the neutron star acquires a cuspy shape. Note also that in principle Gibbs phenomena could be present at the surface of the star even before the mass-shedding limit takes place. This is due to large differences in the density's derivative. However, because the LORENE spectral code adopts a multidomain method and surface-fitting coordinates, on each domain the physical fields are smooth functions and Gibbs phenomena do not appear (see Ref. [50] for detailed explanations).

B. Binding energy and total angular momentum

We plot in Fig. 3 the normalized binding energy, $(M_T - m)/m$, along the quasiequilibrium sequences of binary neutron stars versus the orbital angular frequency. We find that after the onset of dynamical scalarization the binding energy in the scalar-tensor case decreases less rapidly than in general relativity (GR), differing at most by 14% at high frequencies for the cases considered. This implies that binary neutron stars undergoing dynamical scalarization in the DEF theory spiral in more quickly than in general relativity, if the amount of energy flux of gravitational radiation in the scalar-tensor case is equal to the one in general relativity. As we shall see below, the former can be much larger than the latter, so the binary neutron star approaches the merger even more quickly once the energy flux in scalar-tensor theory is also taken into account.

The binding energy is defined by the difference between the tensor mass at a given separation, M_T, and that at infinity, m. The tensor mass is given by the sum of the ADM mass, M_{ADM}, and the scalar mass, M_S [49]. Quite interestingly, we find that the scalar mass is not responsible of the large increase of the tensor mass; the latter increases because of the large increase (three orders of magnitude) of the scalar field in the ADM mass. As seen in Eq. (14a), the scalar field and its derivatives enter the source term of the Poisson-like equation of the conformal factor, which determines the ADM mass.

In Fig. 4 we plot the total angular momentum, $J/(G_N m^2)$, along the quasiequilibrium sequences versus the orbital angular frequency. The behavior of the total angular momentum is basically the same as the binding energy; i.e., after the onset of dynamical scalarization the total angular momentum in the scalar-tensor case decreases less rapidly than in general relativity.

It is worth noticing that in some cases the binding energy/total angular momentum may reach their minimum

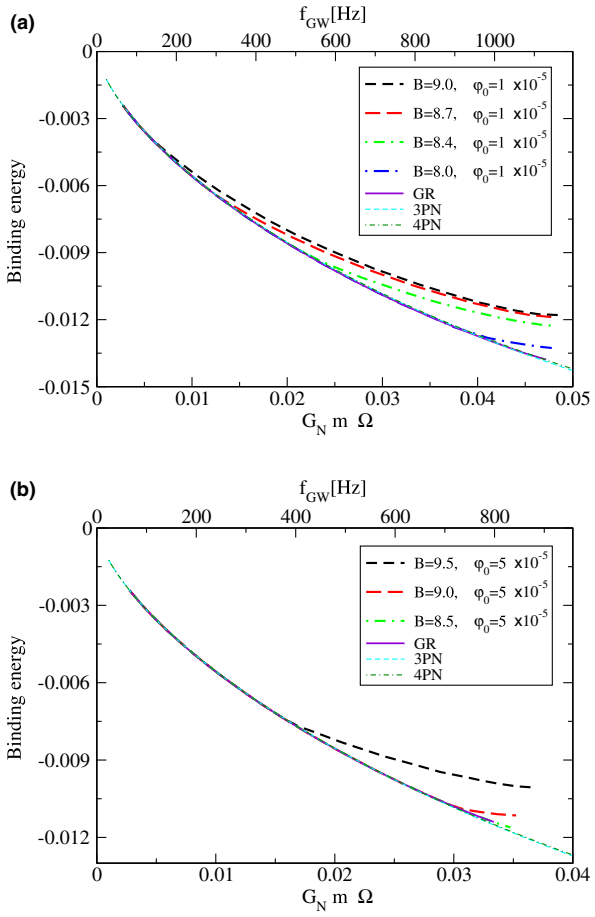

FIG. 3 (color online). Binding energy as a function of the orbital angular frequency normalized to the tensor mass at infinite separation (lower x axis) or as a function of the frequency of GWs from a binary neutron star with $m = 2.7M_\odot$ (upper x axis). Upper panel (a) shows results for APR4 EOS. Black short-dashed, red long-dashed, green dot-short-dashed, and blue dot-long-dashed curves are, respectively, the cases: $B = 9.0$, 8.7, 8.4, and 8.0. Lower panel (b) shows results for H4 EOS. Black short-dashed, red long-dashed, and green dot-dashed curves are, respectively, the cases: $B = 9.5$, 9.0, and 8.5. In both panels, the purple solid curve is drawn by using a quasiequilibrium sequence in general relativity (GR). Cyan dashed and dark-green dot-dashed curves refer to the 3PN and 4PN binding energy in general relativity, respectively [51] (see also Refs. [52–54]). (a) APR4 : $1.35\,M_{sol} - 1.35\,M_{sol}$. (b) H4 : $1.35\,M_{sol} - 1.35\,M_{sol}$.

before the onset of mass shedding. The sequences shown in Figs. 3 and 4 terminate slightly before the onset of mass shedding because it is impossible to treat a cuspy shape within the spectral method, as we mentioned at the end of Sec. III A. In order to calculate at which orbital angular frequency the sequences encounter the mass-shedding point, we compute the sensitive mass-shedding indicator χ,

$$\chi \equiv \frac{(\partial(\ln h)/\partial r)_{eq}}{(\partial(\ln h)/\partial r)_{pole}} \tag{22}$$

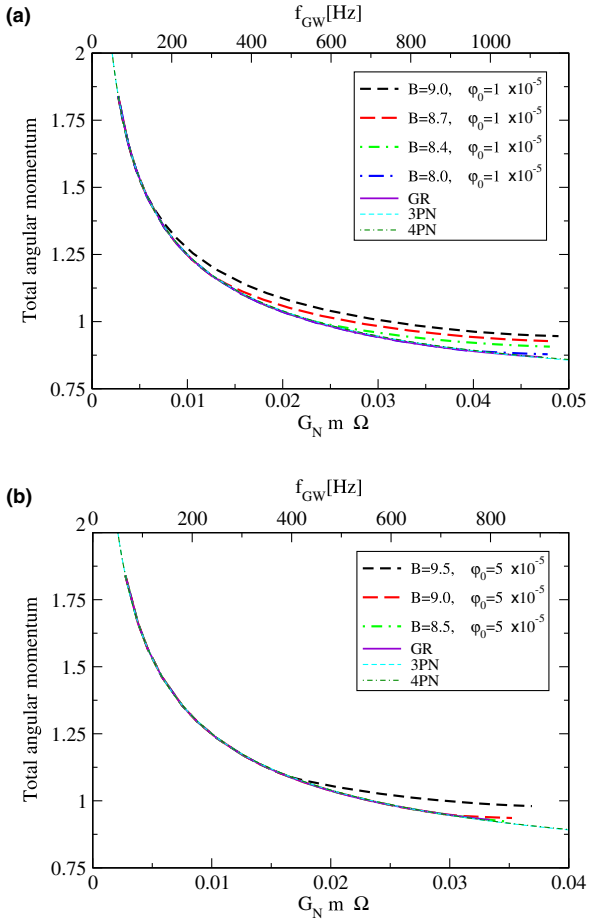

FIG. 4 (color online). Same as Fig. 3 but for the total angular momentum. Cyan dashed and dark-green dot-dashed curves refer to the 3PN and 4PN angular momentum in general relativity, respectively. Those curves are calculated using Refs. [51,55]. (a) APR4: $1.35\,M_{\rm sol} - 1.35\,M_{\rm sol}$. (b) H4: $1.35\,M_{\rm sol} - 1.35\,M_{\rm sol}$.

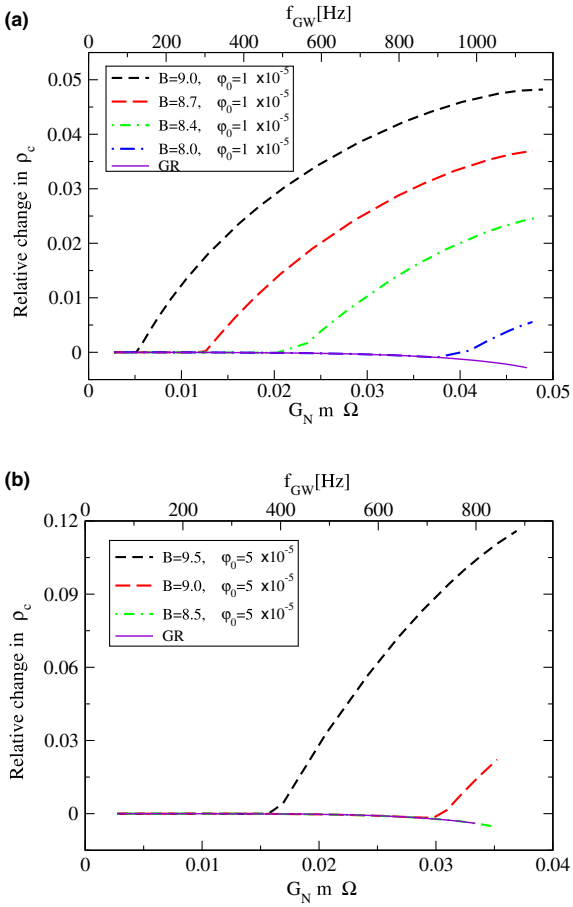

FIG. 5 (color online). Same as Fig. 3 but for the relative change in the central baryonic rest-mass density of a neutron star. (a) APR4: $1.35\,M_{\rm sol} - 1.35\,M_{\rm sol}$. (b) H4: $1.35\,M_{\rm sol} - 1.35\,M_{\rm sol}$.

as a function of the orbital angular frequency. The above quantity is the ratio between the radial derivative of the enthalpy computed in the equatorial plane at the surface along the direction toward the companion star and the one at the surface of the pole of the star. The indicator takes the value $\chi = 1$ for spherical stars and it is $\chi = 0$ in the mass-shedding limit. We extrapolate the sequences of χ to the mass-shedding limit and determine the orbital angular frequency at that point. (For more details on this method see Sec. 4.3 in Ref. [37].) After determining the orbital angular frequency at the onset of mass shedding, we then extrapolate the binding energy curve to that frequency.

By this procedure we find that the sequences of APR4 EOS $B = 9.0$, 8.7, 8.4, 8.0, and H4 EOS $B = 9.5$, $B = 9.0$ reach the minimum of the binding energy (i.e., the onset of secular instability [56]) before the mass shedding. Thus, in these cases the binary neutron stars terminate the quasiequilibrium sequence at that point, and plunge. By contrast the sequence of H4 EOS $B = 8.5$ terminates at the onset of mass shedding.

C. Central baryonic rest-mass density

In general relativity the central baryonic rest-mass density of a neutron star in irrotational binary systems always decreases as the orbital frequency increases (see, e.g., Ref. [47]). We find that this is not the case in the scalar-tensor model under investigation. After the onset of dynamical scalarization, we find that the central baryonic rest-mass density starts increasing (instead of continuing decreasing) as the orbital frequency increases, as shown in Fig. 5. It is not easy to physically explain this behavior because of nonlinear effects related to the deformation of the star and the distribution profiles of metric and matter quantities in the star. In our computation, the baryonic rest mass of each star defined by Eq. (21) is fixed along the quasiequilibrium sequences. To do so, the central value of the baryonic rest-mass density of a neutron star necessarily increases after dynamical scalarization, because the remaining part of Eq. (21) after dropping the rest-mass density,

$$\int_{\rm star\,A} u^t \sqrt{-g} d^3x, \tag{23}$$

decreases rapidly after dynamical scalarization sets in along a constant baryonic rest-mass sequence, while it slightly increases before the dynamical scalarization.

D. Evolution of the orbital angular frequency

We want to estimate the orbital angular frequency and GW cycles in the DEF model assuming a quasistationary adiabatic evolution. We follow what was done in Ref. [37]. Basically, we use the balance equation $dE/dt = -\mathcal{F}$ and integrate $d\Omega/dt = -\mathcal{F}/(dE/d\Omega)$. (Note that this PN approximant is similar to the TaylorT1 approximant in Ref. [57].) For E we use the binding energy [fitted to a polynomial in $x \equiv (G_{\rm N} m\Omega)^{2/3}$] along the quasiequilibrium sequences. The choice of the energy flux $\mathcal{F}$ is less straightforward because we do not know it exactly, so we have to rely on PN calculations [14,20–22,30,58].

Since in this paper we consider only the case of equal-mass binaries on a circular orbit, the monopole and dipole components of the gravitational radiation vanish. Thus, the leading term is the quadrupole component. Using Ref. [20] [see in particular Eqs. (6.40) and (6.41) therein] we find that the ratio of the quadrupole component generated directly by the scalar field, $\mathcal{F}_\varphi^{\rm Quadrupole}$, and the quadrupole component of the gravitational field, $\mathcal{F}_G^{\rm Quadrupole}$, is given at leading order in the PN expansion by[3]

$$\frac{\mathcal{F}_\varphi^{\rm Quadrupole}}{\mathcal{F}_G^{\rm Quadrupole}} = \frac{\alpha_\varphi^2}{6} = \frac{1}{6B}\left(\frac{M_{\varphi,{\rm NS}}}{m_{\rm NS}}\right)^2, \tag{24}$$

where $M_{\varphi,{\rm NS}}$ is the scalar charge of a neutron star, and $m_{\rm NS}$ is the tensor mass of a *spherical* neutron star, i.e., $m_{\rm NS} = m/2 = 1.35 M_\odot$. The quantity α_φ is an auxiliary quantity [19,20] defined by

$$\alpha_\varphi = -\frac{M_{\varphi,{\rm NS,DEF}}}{m_{\rm NS}} = -\frac{1}{\sqrt{B}}\frac{M_{\varphi,{\rm NS}}}{m_{\rm NS}}. \tag{25}$$

Here $M_{\varphi,{\rm NS,DEF}}$ is the scalar charge of a neutron star defined as the monopole part of the field, $\varphi_{\rm DEF}$, which is expanded as $\varphi_{\rm DEF} = \varphi_{0,{\rm DEF}} + M_{\varphi,{\rm NS,DEF}}/r + \mathcal{O}(1/r^2)$ for $r \to \infty$. (Note that the relation between the var-type scalar field in this paper, φ, and that in Ref. [20], $\varphi_{\rm DEF}$, is given by $\varphi = \sqrt{B}\varphi_{\rm DEF}$.)

Because the scalar charge of a binary system is defined as a global quantity, we do not know the scalar charge of the individual stars in the binary system, $M_{\varphi,{\rm NS}}$. As an approximation, we simply take $M_{\varphi,{\rm NS}} \simeq M_\varphi/2$ for the current estimate. From Fig. 1, we find that the ratio Eq. (24) takes the maximum of about 0.028 in the case of APR4 $B = 9.0$ at the end of the sequence. (The scalar charge at that point is about $M_\varphi = 3.3 M_\odot$.) For the other cases the ratio is less than 0.028 throughout the quasiequilibrium sequences. Thus, since $\mathcal{F}_\varphi^{\rm Quadrupole}$ is at most 3% of the quadrupole component of the gravitational field, $\mathcal{F}_G^{\rm Quadrupole}$, we neglect it.

Considering the above, we make the following choices for the gravitational energy flux $\mathcal{F}$ in the balance equation: (i) the 3.5PN flux (also as a polynomial in x) computed in general relativity [5], and (ii) the quadrupole component of the gravitational field in the scalar-tensor DEF model, i.e., $\mathcal{F}_G^{\rm Quadrupole} = (32\nu^2/5)(G_{\rm N} m(1+\alpha_\varphi^2)\Omega)^{10/3}$ where $\nu = m_{\rm NS}^2/m^2$ [11,20]. The choice (i) will allow us to isolate the contribution to the orbital angular frequency (and the number of GW cycles, see below) due to the binding energy computed in this paper, while the choice (ii) is an estimate of the orbital angular frequency when also the gravitational radiation in scalar-tensor theory is included. (Note that today the energy flux in scalar-tensor theory is known only through leading quadrupole order.) In Appendix C, we further discuss those choices and explain how we derive the energy flux in case (ii) using the scalar charge computed in this paper.[4]

In the examples shown in Fig. 6 for the choice (i) and in Fig. 7 for the choice (ii), we set the initial orbital angular frequency to $G_{\rm N} m\Omega = 0.005$ for the case of APR4 EOS and $G_{\rm N} m\Omega = 0.01$ for H4 EOS. The final orbital angular frequency of each curve corresponds to the end point of the quasiequilibrium sequences. As explained above when discussing Fig. 3, the sequences may have the minimum of the binding energy before the mass-shedding point. If the minimum is found, we use the orbital angular frequency at that point, $G_{\rm N} m\Omega_{\text{ener-min}}$, as the final one. If not, we adopt the orbital angular frequency at the mass-shedding limit, $G_{\rm N} m\Omega_{\text{mass-shed}}$, as the final one. In Table II we show the orbital angular frequency at the end point of each model which is used for the final orbital angular frequency. For 3PN and 4PN cases, we use the same final orbital angular frequency as that in general relativity. Note that the final orbital angular frequency listed in Table II is about $G_{\rm N} m\Omega = 0.05$ for APR4 EOS and 0.04 for H4 EOS. These values correspond to the frequency of GWs of $\simeq$1200 Hz and $\simeq$ 960 Hz which lie in the high-frequency portion of the LIGO/Virgo/KAGRA bandwidth. As a consequence, the effects discussed in Secs. III D and III E may not be observable if the broadband noise spectral density is employed. By contrast interferometer configurations optimized at high frequency may allow us to measure these effects.

[3]Here and in the following we assume that the energy flux derived in PN theory expanding the neutron-star masses about the asymptotic value φ_0 continues to be valid also in the presence of spontaneous and/or dynamical scalarization.

[4]We are currently working on long-term evolutions of binary neutron stars extending our previous study [10]. Preliminary analysis shows that the GW energy flux in the scalar-tensor DEF model, at a given orbital frequency, is indeed larger than in the general-relativity case. However, case (ii) seems to overestimate it and the exact GW luminosity is likely to lie between cases (i) and (ii).

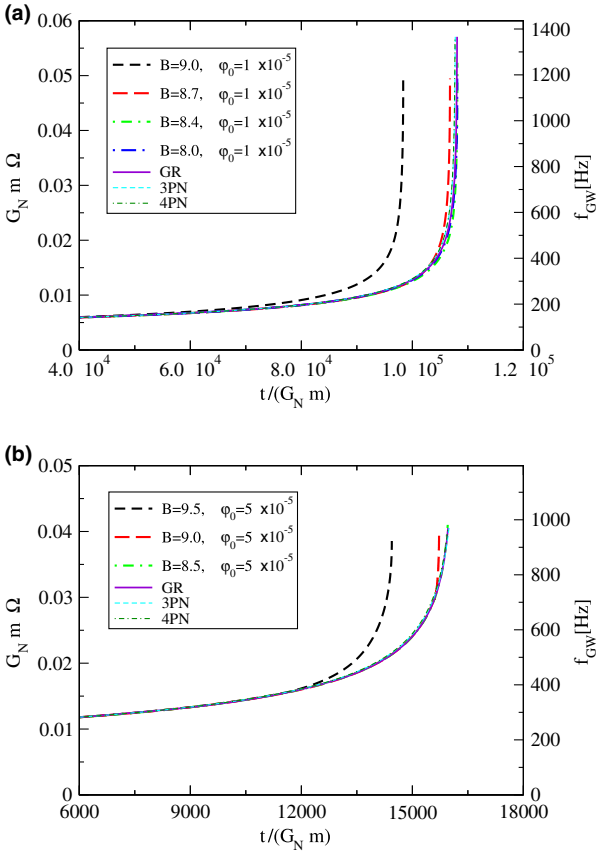

FIG. 6 (color online). Same as Fig. 3 but for the evolution of the orbital angular frequency (left y axis) or the frequency of GWs (right y axis) from a binary neutron star with $m = 2.7M_\odot$. The gravitational energy flux is the choice (i). (a) APR4 : 1.35 M_{sol} − 1.35 M_{sol}. (b) H4 : 1.35 M_{sol} − 1.35 M_{sol}.

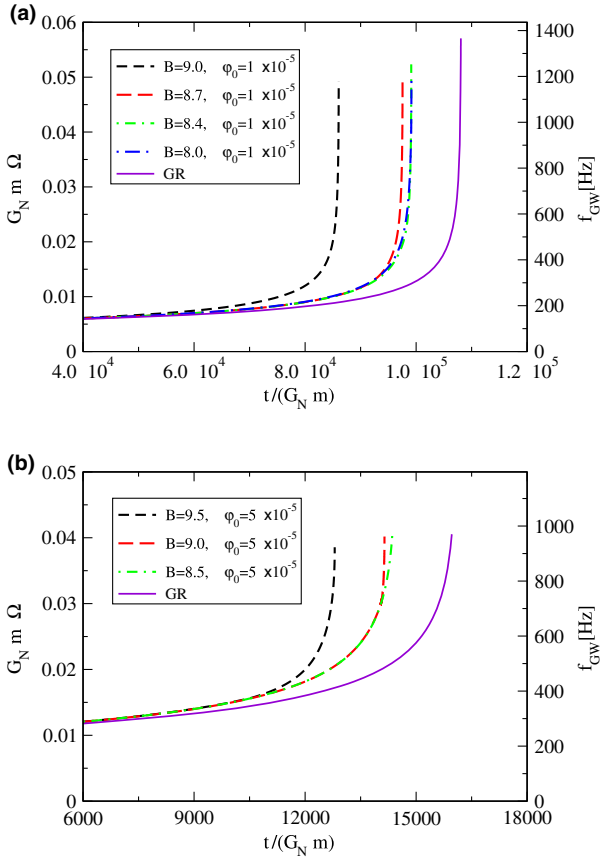

FIG. 7 (color online). Same as Fig. 6 but for the choice (ii) for the gravitational energy flux. In the general-relativity case, the 3.5PN energy flux computed in general relativity is used. These are the same data as used in Fig. 6 (shown as "GR"). (a) APR4 : 1.35 M_{sol} − 1.35 M_{sol}. (b) H4 : 1.35 M_{sol} − 1.35 M_{sol}.

TABLE II. We list the orbital angular frequencies at the end point of each quasiequilibrium sequence and the number of GW cycles. We also show the quantity $\delta\mathcal{N}_{GW}$, which is the difference between the number of GW cycles in the DEF model and in general relativity [i.e., either APR4 (GR) or H4 (GR) depending on the EOS]. When computing the number of cycles, we set the initial orbital angular frequency to $G_N m\Omega = 0.005$ ($f_{GW} = 119.7$ Hz) for the case of APR4 EOS and $G_N m\Omega = 0.01$ ($f_{GW} = 239.3$ Hz) for H4 EOS. The subscripts (i) or (ii) refer to the choice of the gravitational energy flux discussed in Sec. III D.

Models	$G_N m\Omega_{ener\text{-}min}$	$G_N m\Omega_{mass\text{-}shed}$	$\mathcal{N}_{GW(i)}$	$\delta\mathcal{N}_{GW(i)}$	$\mathcal{N}_{GW(ii)}$	$\delta\mathcal{N}_{GW(ii)}$
APR4 (9.0)	0.0491672	0.0565207	238.00	−28.87	202.03	−64.85
APR4 (8.7)	0.0494752	0.0572480	256.62	−10.25	231.48	−35.40
APR4 (8.4)	0.0523407	0.0570327	262.94	−3.93	239.63	−27.24
APR4 (8.0)	0.0494658	0.0563251	265.55	−1.33	242.62	−24.25
APR4 (GR)	···	0.0570651	266.87	···	···	···
APR4 (3PN)	···	···	266.08	−0.79	···	···
APR4 (4PN)	···	···	265.81	−1.07	···	···
H4 (9.5)	0.0385605	0.0438147	62.66	−10.89	54.76	−18.78
H4 (9.0)	0.0401870	0.0419199	70.89	−2.66	63.68	−9.86
H4 (8.5)	···	0.0410100	73.47	−0.07	66.09	−7.46
H4 (GR)	···	0.0405359	73.54	···	···	···
H4 (3PN)	···	···	74.18	0.64	···	···
H4 (4PN)	···	···	74.01	0.46	···	···

It is relevant to point out that if we consider the case of unequal-mass binaries, there exists the dipole component of the scalar GWs. This contribution has the same sign as that of the quadrupole component [20] and increases the energy flux of the scalar GWs. Moreover, if we take into account the infall velocity of the stars in the binary system, the monopole component arises. This also contributes to increase the energy flux of scalar GWs [20]. Thus, since the energy flux increases for unequal-mass binaries, in these cases the merger may occur at even earlier times than what we estimated in Fig. 6.

E. Number of gravitational-wave cycles

As seen in Fig. 3, because after the onset of dynamical scalarization, the binding energy calculated in the DEF model decreases less rapidly than that calculated in general relativity, the binary evolves more quickly in the DEF model than in general relativity, if differences between the energy fluxes in general relativity and scalar-tensor theory are neglected. When an estimate of the scalar-tensor energy flux is included the late evolution of the binary is even faster (see Figs. 6 and 7). As a consequence, the number of GW cycles computed from an initial frequency $f_{\mathrm{GW,ini}}$ to a final frequency $f_{\mathrm{GW,fin}}$ will be different in the DEF model and in general relativity. To quantify this, we numerically integrate the orbital angular frequency between the initial and final frequencies discussed in Table II and the text around it. When computing the number of cycles between two models with the same EOS, we impose that they have the same initial orbital frequency. The results are summarized in Table II and in Figs. 8 and 9. In particular, the difference in number of GW cycles between the DEF model and general relativity for APR4 EOS is 28.9, 10.3, 3.9, and 1.3 for the case of $B = 9.0$, 8.7, 8.4, and 8.0, respectively, if we use the choice (i) for the gravitational energy flux. On the other hand, if we adopt the choice (ii), the difference in number of GW cycles is 64.8, 35.4, 27.2, and 24.3. Note here that the difference is calculated against the general-relativity case with 3.5PN energy flux for both choices of (i) and (ii). For the case of H4 EOS, the difference is 10.9, 2.7, and 0.07 for $B = 9.5$, 9.0, and 8.5, respectively, for the choice (i), while for the choice (ii), we have 18.8, 9.9, and 7.5, respectively. Thus, except for the case of H4 EOS $B = 8.5$ for the choice (i), the difference in number of GW cycles is larger than unity.

However, those numbers should be taken with cautiousness because they are affected by a different source of errors. For example, the quasiequilibrium configurations themselves include errors. It is usually common to measure the errors by a global error indicator, i.e., the error in the virial relation. In scalar-tensor theory the virial relation is expressed as [59]

$$M_{\mathrm{Komar}} = M_{\mathrm{ADM}} + 2M_{\mathrm{S}}\phi_0^{-1}, \tag{26}$$

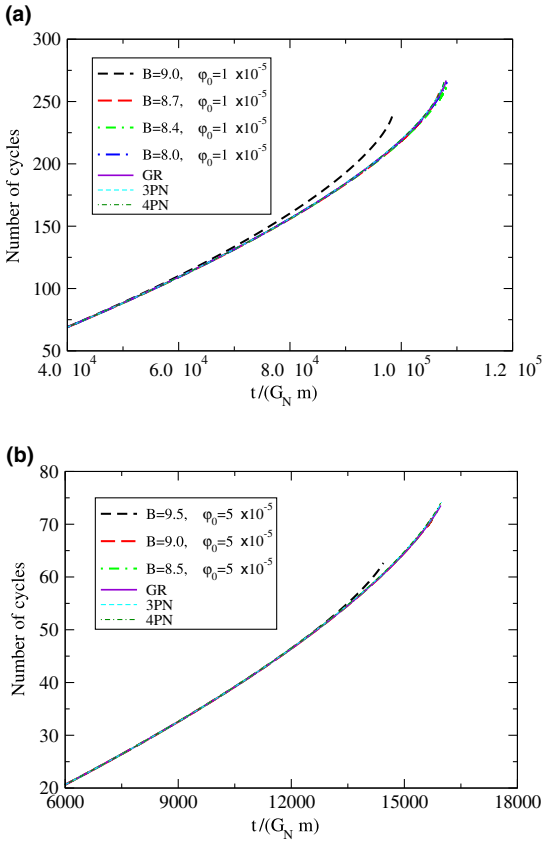

FIG. 8 (color online). Same as Fig. 3 but for the evolution of the number of GW cycles. The gravitational energy flux is the choice (i). (a) APR4 : $1.35\,\mathrm{M_{sol}} - 1.35\,\mathrm{M_{sol}}$. (b) H4 : $1.35\,\mathrm{M_{sol}} - 1.35\,\mathrm{M_{sol}}$.

where M_{Komar} is the Komar mass. This relation should hold along the quasiequilibrium sequences, but because of numerical errors, deviations can appear. In this paper we define the error in the virial relation as follows

$$\text{virial error} = \left| \frac{M_{\mathrm{Komar}} - M_{\mathrm{ADM}} - 2M_{\mathrm{S}}\phi_0^{-1}}{M_{\mathrm{ADM}}} \right|. \tag{27}$$

In our quasiequilibrium configurations the "virial error" is on the order of 10^{-5} for large and medium orbital separations and 10^{-4} for close configurations. Because the binding energy is on the order of $10^{-3} - 10^{-2}$ throughout the computed orbital-frequency range, a virial error on the order of $10^{-5} - 10^{-4}$ implies that the binding energy has a maximal error of a few %. Besides the error in the quasiequilibrium configurations, there are errors due to the fitted curves of the binding energy and the scalar charge. Nevertheless, the difference in the number of cycles in Table II is sufficiently large to make it worthwhile to run accurate, long full numerical-relativity simulations of binary neutron stars in the DEF model and develop accurate template waveforms.

The frequency region that is affected by dynamical scalarization is in the several hundreds of Hz, i.e., in the

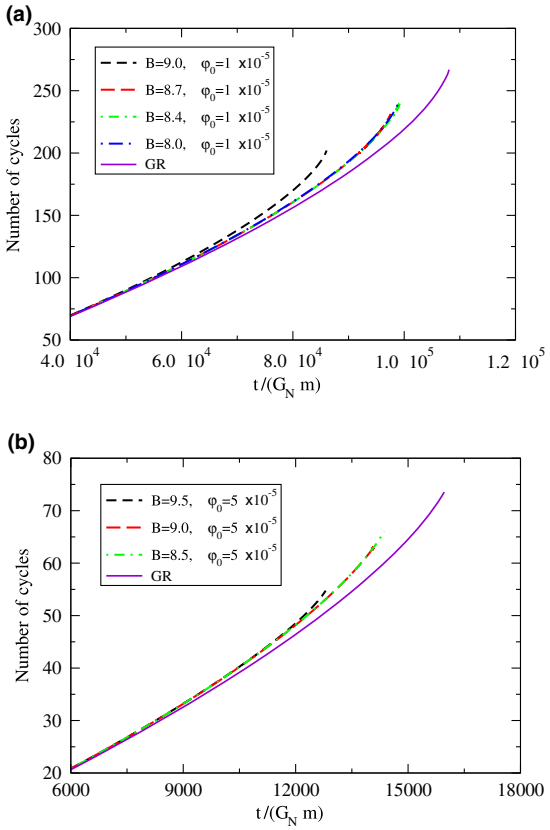

FIG. 9 (color online). Same as Fig. 8 but for the choice (ii) for the gravitational energy flux. In the general-relativity case, the 3.5PN GR energy flux is used. These are the same data used in Fig. 6 (shown as "GR"). (a) APR4: $1.35\,M_{\rm sol} - 1.35\,M_{\rm sol}$. (b) H4: $1.35\,M_{\rm sol} - 1.35\,M_{\rm sol}$.

high-frequency portion of the LIGO/Virgo/KAGRA bandwidth. If the binary is composed by a neutron star and black hole, dynamical scalarization would in principle take place at lower frequencies. Quite interestingly, if the binary is in an eccentric orbit, the motion can induce a scalar charge on the black hole [60]. We plan to study in the future whether dynamical scalarization occurs in a black-hole–neutron-star binary and is observable by LIGO/Virgo/KAGRA.

It is worthwhile to note that the difference in number of GW cycles between the DEF model and general relativity is much larger than that between the 3PN approximation of the binding energy and the 4PN one. (We use the 3.5PN flux for both calculations.) Setting the integration range of $G_{\rm N}m\Omega$ to the same as in the general-relativity case, we obtain that the difference in the number of GW cycles between the 3PN approximation and the 4PN one is 0.28 for APR4 EOS and 0.17 for H4 EOS. (The 4PN case has a smaller number of cycles than that for 3PN.)

Before closing this section, we would like to comment that the difference in GW frequency between general relativity and the DEF model was also estimated in Ref. [11], evolving the 2.5PN equations of motion augmented by a set of equations that phenomenologically describe the increase of scalar charge as the two neutron stars come closer to each other (see Figs. 7, 9, and 11 in Ref. [11]). An important difference between the two sets of results is that the quasiequilibrium sequences in our computation terminate much earlier than those in Ref. [11]. This is because the authors of Ref. [11] treat binary neutron stars as two spherical neutron stars, while we compute the deformation of the stars and stop at the mass-shedding point or at the turning point of the binding energy.

IV. CONCLUSIONS

We have computed quasiequilibrium sequences of binary neutron stars in the DEF scalar-tensor model [19] that admits dynamical scalarization. The EOS of the neutron star that we have employed has the form of a piecewise polytrope and we have used APR4 and H4 EOSs [39,40]. We have considered an equal-mass, irrotational binary whose tensor mass at large separation is $2.7M_\odot$.

Using the quasiequilibrium sequence, we have derived the binding energy and scalar charge and found that, as the stars come closer, and the dynamical scalarization sets in, the binding energy decreases less rapidly than in general relativity. Using the newly computed binding energy and the balance equation, we have estimated the number of GW cycles during the adiabatic, quasicircular inspiral stage up to the end of the sequence, which is the last stable orbit or the mass-shedding point, depending on which comes first. When employing the quadrupole component of the gravitational energy flux in the scalar-tensor DEF model, we have found that in the most optimistic case, when dynamical scalarization sets in around a GW frequency of ~130 Hz (i.e., $B = 9.0$ and APR4 EOS), the number of GW cycles from 120 Hz up to merger in general relativity, ~270, is reduced by 24%, of which 11% is only due to the inclusion of the scalar-tensor binding energy. A summary of our results is given in Table II and Figs. 6–9 for several choices of the scalar-tensor parameters. Of course, a reduction in the number of GW cycles with respect to the general-relativity case does not immediately inform us on whether the deviation can be observed by advanced detectors. An analysis that take into account the noise spectral density of the detector and the accumulated signal-to-noise ratio would be needed [28]. As seen in Table I, GW frequencies at the onset of dynamical scalarization are in the several hundreds of Hz, where the broadband interferometer configuration of LIGO/Virgo/KAGRA has poor sensitivity. In order to measure deviations from general relativity in the DEF model, it is crucial that the scalar-field parameter B be large so that dynamical scalarization sets in at low frequencies (e.g., around 130 Hz for APR4 EOS and $B = 9.0$) and large differences in the GW cycles can be observed. However, if the parameter B were too large, the DEF model would be already rejected by the observational constraints imposed by neutron-star–white-dwarf binaries [44–46].

Recent studies carried out in Refs. [28,61], which use scalar-tensor templates in the frequency domain, rely on the scalar-charge evolution and numerical-relativity simulations of Refs. [9,11], which concluded that advanced detectors operating at a signal-to-noise ratio (SNR) of 10 will be able to constrain dynamical scalarization only if the system scalarizes at low enough orbital frequencies, e.g., ≤ 50 Hz, so that a sufficient number of GW cycles emitted during the dynamical-scalarization phase can contribute to the accumulated SNR. This would imply that in the case of APR4 EOS with $B = 9.0$, advanced LIGO and Virgo might observe deviations from general relativity if dynamical scalarization takes place in nature.

Moreover, using results from Ref. [37] and from GR computations shown in this paper (and also a direct integration of the TaylorT4-PN approximant with tidal effects [62]), we find that in general relativity tidal effects produce a difference of only a few GW cycles (i.e., ~1–3 GW cycles depending on the EOS) between 130 and 1200 Hz with respect to the point-particle case. Those small differences in GW cycles induced by tidal effects at high frequency can be measured by advanced detectors in one single event only if the SNR is roughly 30–35 [63,64]. Note that depending on the EOS those differences can be smaller than or comparable to what we have found in dynamical scalarization (see Table II). At SNR around 30–35, deviations from general relativity might also be observable even in cases in which the onset of dynamical scalarization happens at orbital frequencies above 50 Hz [28,61]. It will be interesting to investigate in the future the detectability of tidal effects in the presence of dynamical scalarization. To precisely determine for which neutron-star masses, EOS, and scalar-tensor parameters dynamical scalarization and tidal effects can be observed with advanced GW detectors, it will be relevant to develop accurate waveforms in the DEF scalar-tensor model. To this respect the next work [65] is focusing at building accurate analytical templates that can incorporate dynamical scalarization, and reproduce the binding energy computed in this paper and the results from numerical-relativity simulations.

Finally, extending earlier work [10], new long-term numerical simulations in scalar-tensor theory are suggesting that the analytical energy flux used in this paper (i.e., the energy flux at quadrupolar order) is likely to overestimate the exact energy flux in the scalar-tensor DEF model. Thus, a better modeling of the energy flux (e.g., its PN computation through 1PN and even 2PN order [58]) is crucial for understanding and quantifying differences from the general-relativity case.

ACKNOWLEDGMENTS

A. B. thanks Noah Sennett for useful discussions on dynamical scalarization. K. T. acknowledges partial support from JSPS Grant-in-Aid for Scientific Research (26400267). M. S. acknowledges partial support from JSPS Grant-in-Aid for Scientific Research (24244028), JSPS Grant-in-Aid for Scientific Research on Innovative Area (20105004), and HPCI Strategic Program of Japanese MEXT. A. B. acknowledges partial support from NSF Grant No. PHY-1208881 and NASA Grant No. NNX12AN10G.

APPENDIX A: QUASIEQUILIBRIUM SEQUENCES OF BINARY SYSTEMS WITH A POLYTROPIC EQUATION OF STATE

In this Appendix, we work within the DEF scalar-tensor theory and compute quasiequilibrium sequences for two models of binary neutron stars with a polytropic equation of state, $P = \kappa\rho^{\Gamma}$, where κ is a constant.[5] The adiabatic index, Γ, is set to 2 and the polytropic constant, κ, is to 0.0332278 in units of $c^2/\rho_{\rm nuc}$, where $\rho_{\rm nuc}$ is the nuclear density defined in LORENE [29]. This value of the polytropic constant κ is the same as the one used for the initial data with $\Gamma = 2$ that can be downloaded from the LORENE website [29]. When we employ physical quantities used in LORENE (which are in SI units but here we translate them in cgs units), the nuclear density $\rho_{\rm nuc} = 1.66 \times 10^{14}$ [g/cm^3], Newton's constant $G_{\rm N} = 6.6726 \times 10^{-8}$[cm^3/gs^2], the speed of light $c = 2.99792458 \times 10^{10}$ [cm/s], and the solar mass $M_\odot = 1.989 \times 10^{33}$ [g], the polytropic constant $\kappa = 0.0332278[c^2/\rho_{\rm nuc}]$ is written as $\kappa/c^2 = 123.641 G^3 M_\odot^2/c^6$. This value is slightly larger than the one used by Barausse *et al.* [9] which is $123 G^3 M_\odot^2/c^6$. (Note that, recently, after our computations finished, the units in the LORENE code have been updated. As a consequence the fundamental units that we list above differ from the ones in the LORENE code by 10^{-4}.)

We will study the same binary configurations considered in Ref. [9]. However, whereas Ref. [9] computed the initial data in general relativity, we calculate them in the DEF scalar-tensor theory. In order to set the values of B and φ_0, we need to derive relations between quantities used by Barausse *et al.* [9] and Shibata *et al.* [10]. We will do it using definitions introduced by Damour and Esposito-Farèse [19]. We use the subscript DEF for Damour and Esposito-Farése, BPPL for Barausse *et al.*, and STOB for Shibata *et al.*

As given in Ref. [9], the relation between $\varphi_{\rm BPPL}$ and $\varphi_{\rm DEF}$ is $\varphi_{\rm BPPL} = \varphi_{\rm DEF}/\sqrt{4\pi G}$, and the var-type scalar field is related to the scalar field ϕ as $\phi = \exp(-\beta\varphi_{\rm BPPL}^2)$, where β is a constant. On the other hand, the relation between $\varphi_{\rm STOB}$ and $\varphi_{\rm DEF}$ is $\varphi_{\rm STOB} = \sqrt{B}\varphi_{\rm DEF}$, and the var-type scalar field is related to the scalar field as $\phi = \exp(\varphi_{\rm STOB}^2/2)$ [10]. From these equations we conclude that the relations between the definitions by Barausse *et al.* [9] and Shibata *et al.* [10] are

[5]Note that the relation between κ and K, which is the polytropic constant defined in Ref. [9], is $\kappa = Kc^2$.

$$B = -2\left(\frac{\beta}{4\pi G}\right), \tag{A1}$$

$$\varphi_{\rm STOB} = \sqrt{4\pi G B}\varphi_{\rm BPPL}. \tag{A2}$$

Thus, the parameters used by Barausse *et al.*, $\beta/(4\pi G) = -4.5$ and $(\varphi_{\rm BPPL})_0 = 10^{-5}G^{-1/2}$, correspond to $B = 9.0$ and $(\varphi_{\rm STOB})_0 = \sqrt{4\pi B}\times 10^{-5} = 6\sqrt{\pi}\times 10^{-5}$ in this paper. For simplicity, in the following we drop "STOB" from $\varphi_{\rm STOB}$.

Fixing the quantities B and φ_0 to the above values, we compute two configurations of binary neutron stars. The first one describes an unequal-mass binary in which the baryonic rest masses of each star are $1.78M_\odot$ and $1.90M_\odot$, respectively. The gravitational masses of spherical stars having the same baryonic rest masses are $1.64M_\odot$ (with compactness 0.160) and $1.74M_\odot$ (with compactness 0.181). Thus, the tensor mass at infinite separation is $m = 3.39M_\odot$. The more massive star is spontaneously scalarized when it is a spherical (isolated) star, and it has the scalar charge of $0.790M_\odot$ and the scalar mass of $4.20\times 10^{-5}M_\odot$. On the other hand, the less massive star is not spontaneously scalarized in a spherical (isolated) state and has the scalar charge of $0.0117M_\odot$ and the scalar mass of $6.22\times 10^{-7}M_\odot$. Because of the more massive star's scalar field, the binary system is already scalarized as demonstrated in Fig. 10 (note the vertical axis in the figure is in linear scale). As discussed in Sec. I, because the binary system is already scalarized, the general-relativity initial data used in this case by Barausse *et al.* have artificially put the binary system in a local minimum of the binding energy. Thus, we suspect that the fast plunge seen by Barausse *et al.* might be enhanced by this effect. It would be interesting to repeat the simulation using initial data in the DEF scalar-tensor theory.

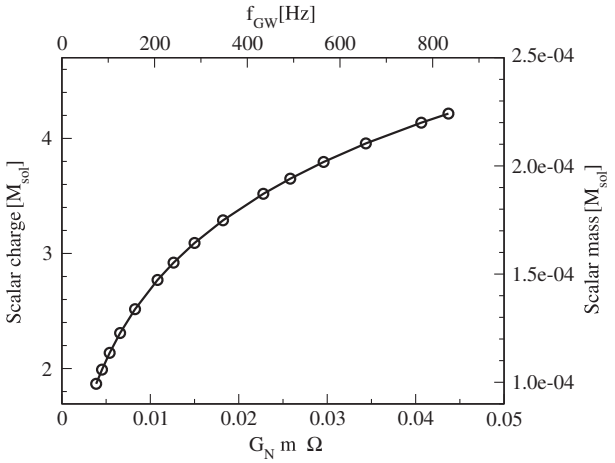

FIG. 10. Scalar charge (left y axis) or scalar mass (right y axis) as a function of the orbital angular frequency normalized to the tensor mass at infinite separation (lower x axis) or as a function of the frequency of GWs defined by $f_{\rm GW} \equiv \Omega/\pi$ from an unequal-mass binary neutron star with $m = 3.39M_\odot$ (upper x axis). The equation of state is a polytropic one with $\Gamma = 2$. Note that the vertical axis is in a linear scale.

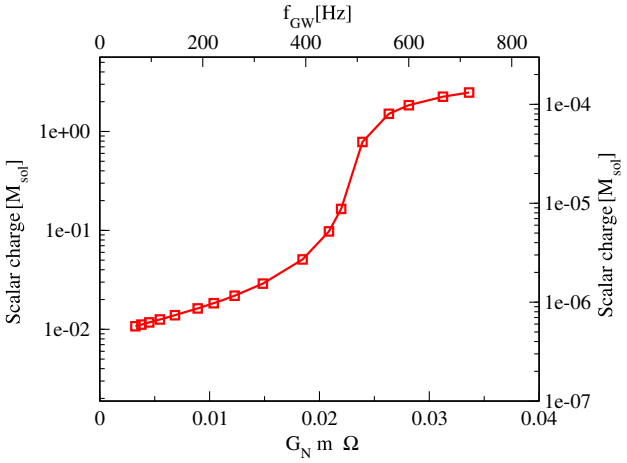

FIG. 11 (color online). Same as Fig. 10 but for an equal-mass binary neutron star with $m = 3.03M_\odot$. Note that the vertical axis is in a logarithmic scale.

The other configuration that we consider is an equal-mass binary in which the baryonic rest mass of both stars is $1.625M_\odot$. The gravitational mass of a spherical star with the same baryonic rest mass is $1.51M_\odot$ and the compactness is 0.140. The tensor mass at infinite separation is $m = 3.03M_\odot$. The star is not spontaneously scalarized in a spherical (isolated) state. Its scalar charge is $4.00\times 10^{-3}M_\odot$ and the scalar mass is $2.13\times 10^{-7}M_\odot$. So, the binary system is not spontaneously scalarized at infinite separation. As shown in Fig. 11, when using the quasiequilibrium sequence, the dynamical scalarization sets in at around the GW frequency of $f_{\rm GW}\sim 450$ Hz. Barausse *et al.* reported that the dynamical scalarization occurs at the GW frequency of $f\sim 645$ Hz. Although this value is slightly larger than ours, those results are consistent. Indeed, we found [10] that the occurrence of dynamical scalarization in a dynamical simulation tends to be delayed compared with that in a quasiequilibrium sequence. This might be due to the infall motion in the simulation.

APPENDIX B: CONVERGENCE TEST FOR THE SCALAR MASS

In this Appendix, we compare the scalar mass of APR4 $B = 8.7$ at orbital angular frequency of $G_{\rm N}m\Omega = 0.00754$ and 0.0206 for different resolutions (i.e., for different number of collocation points). Those orbital angular frequencies are before and after dynamical scalarization. We choose five resolutions, $N_r\times N_\theta\times N_{\hat\varphi} = 49\times 37\times 36$, $41\times 33\times 32$, $33\times 25\times 24$, $25\times 17\times 16$, and $17\times 13\times 12$, where N_r, N_θ, and $N_{\hat\varphi}$ are the number of collocation points for the radial, polar, and azimuthal directions, respectively.

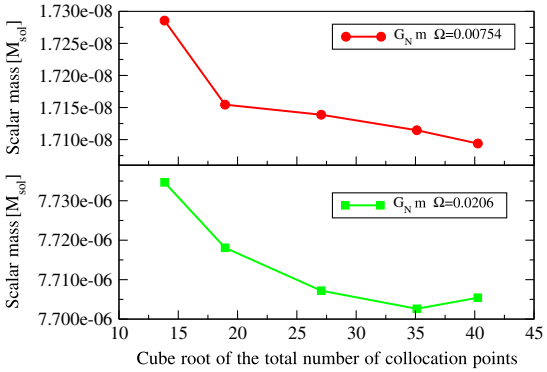

FIG. 12 (color online). Scalar mass of APR4 $B = 8.7$ as a function of the cube root of the total number of collocation points, $\sqrt[3]{N_r \times N_\theta \times N_{\hat{\varphi}}}$. The upper panel is the scalar mass at orbital angular frequency of $G_N m\Omega = 0.00754$, and the lower one is for $G_N m\Omega = 0.0206$. APR4 B $= 8.7\,\mathrm{:}\,1.35\,\mathrm{M_{sol}} - 1.35\,\mathrm{M_{sol}}$.

Figure 12 shows the scalar mass of APR4 $B = 8.7$ as a function of the cube root of the total number of collocation points, $\sqrt[3]{N_r \times N_\theta \times N_{\hat{\varphi}}}$. We find that the scalar mass for $33 \times 25 \times 24$ ($\sqrt[3]{N_r \times N_\theta \times N_{\hat{\varphi}}} \simeq 27.05$) is in approximately convergent level for the case of $G_N m\Omega = 0.0206$ (the case after dynamical scalarization). The relative deviation from the values for higher resolutions is less than 1×10^{-3}. For the case of $G_N m\Omega = 0.00754$ (the case before dynamical scalarization), the resolution of $33 \times 25 \times 24$ seems to be not enough because the orbital separation is twice larger than the case of $G_N m\Omega = 0.0206$. However, the relative deviation of the result for $33 \times 25 \times 24$ from higher resolutions is on the order of a few $\times 10^{-3}$ in 1.7×10^{-8}.

From those convergence tests and to save computational time for our limiting resources, we decide to choose the number of collocation points of $33 \times 25 \times 24$. For much closer cases just before the end of quasiequilibrium sequences, we use $33 \times 21 \times 20$ and $33 \times 17 \times 16$, keeping the number of collocation points for the radial direction.

APPENDIX C: ON THE GRAVITATIONAL-WAVE ENERGY FLUX

In this Appendix, we first explain how we compute the energy flux used in case (ii) (see discussion in Sec. III D),

$$\mathcal{F}_{\mathrm{G}}^{\mathrm{Quadrupole}} = \frac{32}{5}\nu^2[G_N m\Omega(1+\alpha_\varphi^2)]^{10/3}, \tag{C1}$$

and then we compare it to the 3.5PN flux in general relativity [5].

Quite interestingly, by plotting the function $(1+\alpha_\varphi^2)^{10/3}$ that appears in Eq. (C1) versus $x \equiv (G_N m\Omega)^{2/3}$ (see Fig. 13), we find that it can be well approximated by the following simple fit

$$(1+\alpha_\varphi^2)^{10/3} = \begin{cases} 1 & \text{before dyn scal} \\ a_0 + a_1 x & \text{after dyn scal} \end{cases} \tag{C2}$$

where a_0 and a_1 are constants obtained fitting the curves in Fig. 13 after dynamical scalarization. As seen in Fig. 1, the case of H4 EOS $B = 8.0$ does not reach dynamical scalarization; thus, in this case we do not use Eq. (C2), but adopt a polynomial fit in x. Furthermore, by taking the inverse of Eq. (C2), we can express the scalar charge after dynamical scalarization through the analytic formula

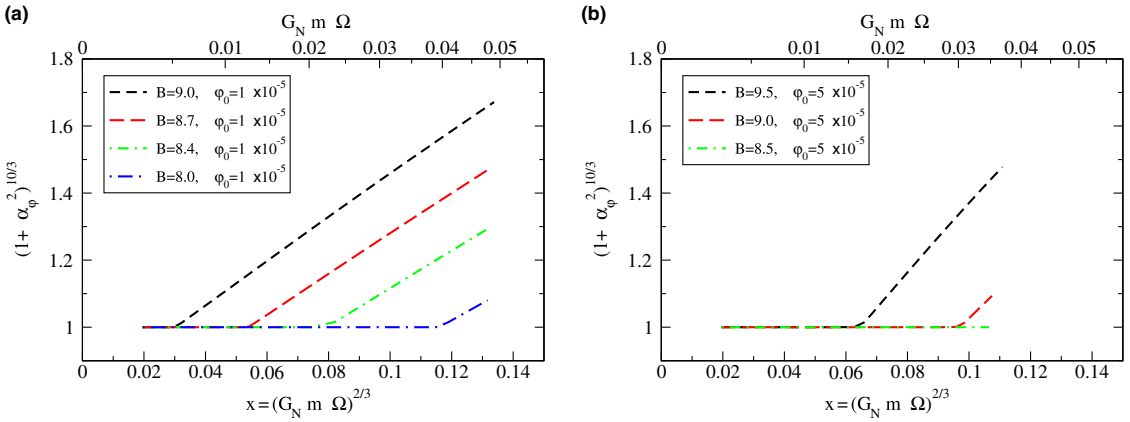

FIG. 13 (color online). We plot the function $(1+\alpha_\varphi^2)^{10/3}$ that appears in Eq. (C1) versus $x \equiv (G_N m\Omega)^{2/3}$ (lower x axis) and the orbital angular frequency normalized to the tensor mass at infinite separation (upper x axis). Left panel (a) shows results for APR4 EOS. Black short-dashed, red long-dashed, green dot-short-dashed, and blue dot-long-dashed curves are, respectively, the cases: $B = 9.0$, 8.7, 8.4, and 8.0. Right panel (b) shows results for H4 EOS. Black short-dashed, red long-dashed, and green dot-dashed curves are, respectively, the cases: $B = 9.5$, 9.0, and 8.5. (a) APR4 : $1.35\,\mathrm{M_{sol}} - 1.35\,\mathrm{M_{sol}}$. (b) H4 : $1.35\,\mathrm{M_{sol}} - 1.35\,\mathrm{M_{sol}}$.

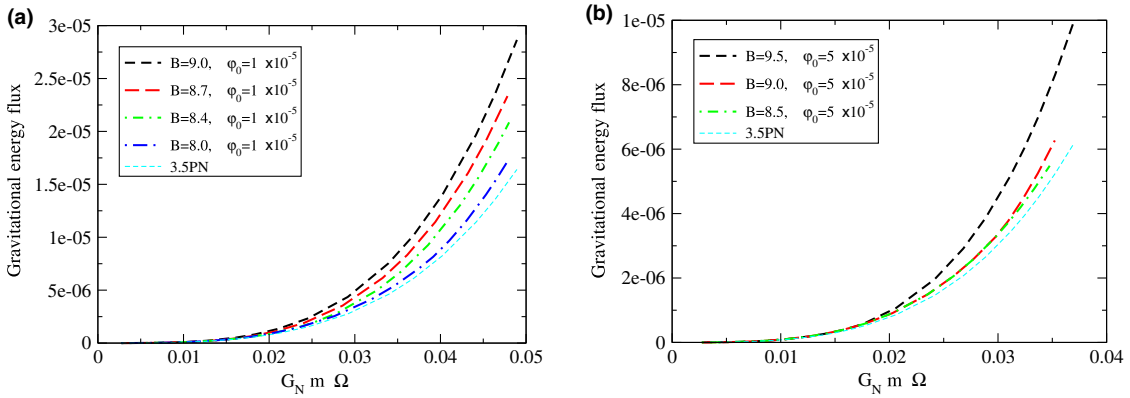

FIG. 14 (color online). Gravitational-wave energy flux as a function of the orbital angular frequency normalized to the tensor mass at infinite separation. Left panel (a) shows results for APR4 EOS. Black short-dashed, red long-dashed, green dot-short-dashed, and blue dot-long-dashed curves are, respectively, the cases: $B = 9.0$, 8.7, 8.4, and 8.0. Right panel (b) shows results for H4 EOS. Black short-dashed, red long-dashed, and green dot-dashed curves are, respectively, the cases: $B = 9.5$, 9.0, and 8.5. Those results are calculated by using Eq. (C1). In both panels, the cyan dashed curve refers to the 3.5PN energy flux in general relativity. (a) APR4 : $1.35\,M_{\rm sol} - 1.35\,M_{\rm sol}$. (b) H4 : $1.35\,M_{\rm sol} - 1.35\,M_{\rm sol}$.

$$M_\varphi = m\sqrt{B}[(a_0 + a_1 x)^{3/10} - 1]^{1/2}. \tag{C3}$$

Finally, using the above results and Eq. (25), we plot in Fig. 14 $\mathcal{F}_{\rm G}^{\rm Quadrupole}$ and the 3.5PN energy flux in general relativity. As we can see, depending on the scalar-tensor parameters, the fractional difference between $\mathcal{F}_{\rm G}^{\rm Quadrupole}$ and the general-relativity flux can become 70%. However, as pointed out in Sec. III A, dynamical scalarization in quasiequilibrium configurations occurs earlier than in numerical simulations [10]. Moreover the increase in scalar charge computed in the simulations is smaller than that obtained in quasiequilibrium study. These facts suggest that the value of the energy flux in case (ii) is likely an overestimate of the exact result. Indeed, as explained in the footnote in Sec. III D, the energy flux obtained in long-term simulations seems to lie between cases (i) and (ii).

[1] J. Abadie *et al.*, Nucl. Instrum. Methods Phys. Res., Sect. A **624**, 223 (2010).
[2] T. Accadia *et al.*, Classical Quantum Gravity **28**, 025005 (2011).
[3] K. Kuroda *et al.*, Classical Quantum Gravity **27**, 084004 (2010).
[4] R. Narayan, B. Paczynski, and T. Piran, Astrophys. J. **395**, L83 (1992).
[5] L. Blanchet, Living Rev. Relativity **9**, 4 (2006).
[6] K. Hotokezaka, K. Kyutoku, H. Okawa, M. Shibata, and K. Kiuchi, Phys. Rev. D **83**, 124008 (2011).
[7] K. Hotokezaka, K. Kiuchi, K. Kyutoku, T. Muranushi, Y. Sekiguchi, M. Shibata, and K. Taniguchi, Phys. Rev. D **88**, 044026 (2013).
[8] S. Bernuzzi, T. Dietrich, W. Tichy, and B. Bruegmann, Phys. Rev. D **89**, 104021 (2014).
[9] E. Barausse, C. Palenzuela, M. Ponce, and L. Lehner, Phys. Rev. D **87**, 081506 (2013).
[10] M. Shibata, K. Taniguchi, H. Okawa, and A. Buonanno, Phys. Rev. D **89**, 084005 (2014).
[11] C. Palenzuela, E. Barausse, M. Ponce, and L. Lehner, Phys. Rev. D **89**, 044024 (2014).
[12] C. M. Will, Living Rev. Relativity **9**, 3 (2006).
[13] C. M. Will, *Theory and Experiment in Gravitational Physics* (Cambridge University Press, Cambridge, England, 1993).
[14] C. M. Will and H. W. Zaglauer, Astrophys. J. **346**, 366 (1989).
[15] P. Jordan, Nature (London) **164**, 637 (1949).
[16] M. Fierz, Helv. Phys. Acta **29**, 128 (1956).
[17] C. Brans and R. H. Dicke, Phys. Rev. **124**, 925 (1961).
[18] Y. Fujii and K. Maeda, *The Scalar-Tensor Theory of Gravitation* (Cambridge University Press, Cambridge, England, 2003).
[19] T. Damour and G. Esposito-Farèse, Phys. Rev. Lett. **70**, 2220 (1993).
[20] T. Damour and G. Esposito-Farèse, Classical Quantum Gravity **9**, 2093 (1992).
[21] T. Damour and G. Esposito-Farèse, Phys. Rev. D **54**, 1474 (1996).
[22] T. Damour and G. Esposito-Farèse, Phys. Rev. D **58**, 042001 (1998).
[23] D. D. Doneva, S. S. Yazadjiev, N. Stergioulas, and K. D. Kokkotas, Phys. Rev. D **88**, 084060 (2013).
[24] P. Pani and E. Berti, Phys. Rev. D **90**, 024025 (2014).

[25] D. D. Doneva, S. S. Yazadjiev, N. Stergioulas, K. D. Kokkotas, and T. M. Athanasiadis, Phys. Rev. D **90**, 044004 (2014).
[26] T. Damour and K. Nordtvedt, Phys. Rev. Lett. **70**, 2217 (1993).
[27] T. Damour and K. Nordtvedt, Phys. Rev. D **48**, 3436 (1993).
[28] L. Sampson, N. Yunes, N. Cornish *et al.*, arXiv:1407.7038 [Phys. Rev. D (to be published)].
[29] http://www.lorene.obspm.fr/.
[30] S. Mirshekari and C. M. Will, Phys. Rev. D **87**, 084070 (2013).
[31] J. W. York, Phys. Rev. Lett. **82**, 1350 (1999).
[32] H. P. Pfeiffer and J. W. York, Phys. Rev. D **67**, 044022 (2003).
[33] J. A. Isenberg (unpublished).
[34] J. A. Isenberg, Int. J. Mod. Phys. D **17**, 265 (2008).
[35] J. R. Wilson and G. J. Mathews, in *Frontiers in Numerical Relativity*, edited by C. R. Evans, L. S. Finn, and D. W. Hobill (Cambridge University Press, Cambridge, England, 1989).
[36] E. Gourgoulhon, P. Grandclément, K. Taniguchi, J.-A. Marck, and S. Bonazzola, Phys. Rev. D **63**, 064029 (2001).
[37] K. Taniguchi and M. Shibata, Astrophys. J. Suppl. **188**, 187 (2010).
[38] E. Gourgoulhon, *3+1 Formalism in General Relativity* (Springer, New York, 2012).
[39] J. S. Read, B. D. Lackey, B. J. Owen, and J. L. Friedman, Phys. Rev. D **79**, 124032 (2009).
[40] J. S. Read, C. Markakis, M. Shibata, K. Uryū, J. D. E. Creighton, and J. L. Friedman, Phys. Rev. D **79**, 124033 (2009).
[41] A. Akmal, V. R. Pandharipande, and D. G. Ravenhall, Phys. Rev. C **58**, 1804 (1998).
[42] B. D. Lackey, M. Nayyar, and B. J. Owen, Phys. Rev. D **73**, 024021 (2006).
[43] C. S. Kochanek, Astrophys. J. **398**, 234 (1992).
[44] P. C. C. Freire, N. Wex, G. Esposito-Farèse, J. P. W. Verbiest, M. Bailes, B. A. Jacoby, M. Kramer, I. H. Stairs, J. Antoniadis, and G. H. Janssen, Mon. Not. R. Astron. Soc. **423**, 3328 (2012).
[45] J. Antoniadis *et al.*, Science **340**, 1233232 (2013).
[46] N. D. R. Bhat, M. Bailes, and J. P. W. Verbiest, Phys. Rev. D **77**, 124017 (2008).
[47] K. Taniguchi and E. Gourgoulhon, Phys. Rev. D **66**, 104019 (2002).
[48] K. Taniguchi and E. Gourgoulhon, Phys. Rev. D **68**, 124025 (2003).
[49] D. L. Lee, Phys. Rev. D **10**, 2374 (1974).
[50] S. Bonazzola, E. Gourgoulhon, and J.-A. Marck, Phys. Rev. D **58**, 104020 (1998).
[51] D. Bini and T. Damour, Phys. Rev. D **87**, 121501 (2013).
[52] E. Barausse, A. Buonanno, and A. Le Tiec, Phys. Rev. D **85**, 064010 (2012).
[53] P. Jaranowski and G. Schäfer, Phys. Rev. D **86**, 061503 (2012).
[54] P. Jaranowski and G. Schäfer, Phys. Rev. D **87**, 081503 (2013).
[55] A. Le Tiec, L. Blanchet, and B. F. Whiting, Phys. Rev. D **85**, 064039 (2012).
[56] J. L. Friedman, K. Uryū, and M. Shibata, Phys. Rev. D **65**, 064035 (2002).
[57] M. Boyle, D. Brown, L. Kidder, A. Mroué, H. Pfeiffer, M. Scheel, G. Cook, and S. Teukolsky, Phys. Rev. D **76**, 124038 (2007).
[58] R. N. Lang, Phys. Rev. D **89**, 084014 (2014).
[59] M. Shibata and K. Kawaguchi, Phys. Rev. D **87**, 104031 (2013).
[60] K. Liu, R. P. Eatough, N. Wex, and M. Kramer, Mon. Not. R. Astron. Soc. **445**, 3115 (2014).
[61] L. Sampson, N. Cornish, and N. Yunes, Phys. Rev. D **89**, 064037 (2014).
[62] T. Hinderer (private communication).
[63] W. Del Pozzo, T. G. F. Li, M. Agathos, C. Van Den Broeck, and S. Vitale, Phys. Rev. Lett. **111**, 071101 (2013).
[64] L. Wade, J. D. E. Creighton, E. Ochsner, B. D. Lackey, B. F. Farr, T. B. Littenberg, and V. Raymond, Phys. Rev. D **89**, 103012 (2014).
[65] N. Sennett, A. Buonanno, M. Shibata, and K. Taniguchi (to be published).